

Initial Clinical Experience Utilizing 4D-MRI for Radiation Treatment Planning

Eric S. Paulson^{1,3}; Nikolai J. Mickevicius^{1,3}

Departments of ¹Radiation Oncology, ²Radiology, and ³Biophysics, Medical College of Wisconsin, Milwaukee, WI, USA

Introduction

Knowledge of target and organ at risk (OAR) motion trajectories is essential in radiation therapy. Motion can result in a smearing of planned dose distributions, particularly when steep dose gradients are employed to reduce radiation doses to proximal OARs [1]. This can result in an inevitable disconnect between planned and actual doses delivered to targets and OARs over the course of treatment.

Motion management in radiation therapy involves two components: 1) generation of high-fidelity static images of targets and OARs along with models of respiratory motion for use in treatment *planning*, 2) real-time intrafraction motion monitoring for exception gating and/or tracking during treatment *delivery* [1]. Currently, the clinical standard-of-care to address the former relies on four-dimensional (4D) computed tomography (CT) images of the patient [2]. However, the poor soft tissue contrast can challenge accurate target and OAR delineation in some cancer sites with CT [3] and, thus, the accuracy of motion models obtained with this approach. Consequently, larger margins are often prescribed to prevent underdosing of tumor targets [1, 4].

Due to its non-ionizing and high soft tissue contrast properties, magnetic resonance imaging (MRI) is an ideal 4D-imaging platform. A multitude of 4D-MRI strategies have been explored in the literature, utilizing prospective and retrospective acquisitions of multi-slice 2D or 3D excitations with Cartesian and non-Cartesian readouts and a variety of motion surrogates [5–15]. Recently, self-navigated, under-sampled, retrospectively sorted 3D volumetric acquisitions have been introduced for 4D-MRI. Although long acquisition and reconstruction times (up to 8 minutes and several hours, respectively) have been reported with some of these methods, the 3D radial stack-of-stars method [12–15] offers great potential to minimize acquisition and reconstruction times while maintaining image quality. In addition, the method facilitates ease of extracting motion surrogates and is robust against motion artifacts from the inherent properties of radial k -space trajectories. We discuss here our initial clinical experience performing and utilizing 4D-MRI for radiation treatment planning.

Methods

Patients undergoing MR simulation for radiotherapy of abdominal or thoracic cancers were imaged with 4D-MRI after providing informed written consent under guidelines established by the IRB at our Institution. Following CT simulation, patients were transferred to a 3T MAGNETOM Verio scanner (Siemens Healthcare, Erlangen, Germany) and set up in treatment position on a flat table overlay. Two 6-channel flexible array coils were wrapped around the anterior of the patient and suspended on expandable RF coil bridges. Combined with the spine array, between 21 and 24 receive coils were used for imaging. Per standard MR simulation protocols at our Institution, glucagon (1 mg, Novo Nordisk, Bagsværd, Denmark) was administered intravenously in abdominal cancer patients to reduce peristalsis. Post-contrast imaging was performed following administration of Eovist (10 mL, Bayer Healthcare, Berlin, Germany) for cholangiocarcinoma patients, or Multihance (0.1 mmol/kg, Bracco Imaging, Milano, Italy).

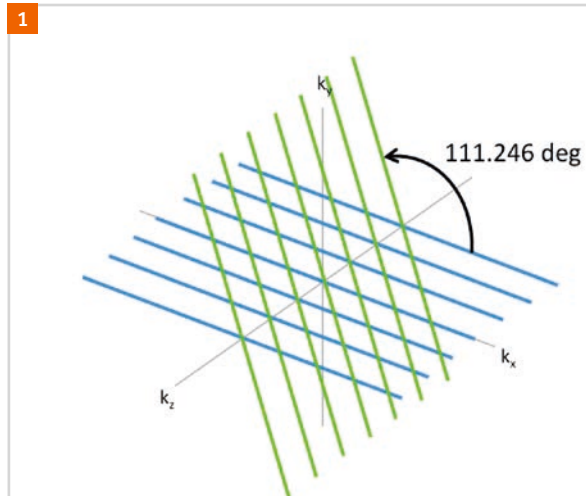


Figure 1: Hybrid 3D golden angle radial stack of stars trajectory. All partitions defining a spoke-plane are acquired before incrementing the spoke angle.

4D-MRI acquisition

A hybrid, slab-selective, 3D radial VIBE sequence of our own design was implemented for 4D-MRI. The sequence supports switchable FLASH, FISP, TrueFISP, and PSIF modes for T1 and mixed T2/T1-weighted contrasts. A 3-point Dixon readout, integrated into the sequence, is available for FLASH and FISP modes. Cartesian encoding of partitions is performed along the slab-select direction (k_z) for a given spoke angle, forming a spoke-plane. After acquisition of the prescribed partitions within the spoke-plane, the spoke angle is incremented by the golden angle ($\pi \times \text{golden ratio} = 111.246^\circ$) and another spoke-plane is acquired (Fig. 1). This process is repeated for the entire scan duration. In this manner, a unique spoke is sampled throughout the entire duration of the acquisition, eliminating the need to complex average overlapping spokes after the k -space data are retrospectively sorted into respiratory phases. Typical 4D-MRI scan parameters included: axial prescription, field-of-view: 330 mm, base resolution: 192, readout bandwidth: 200 kHz, TE/TR: 1.3/3.5 msec, flip angle: 10° , slab thickness: 240 mm, total acquisition time: 2 minutes.

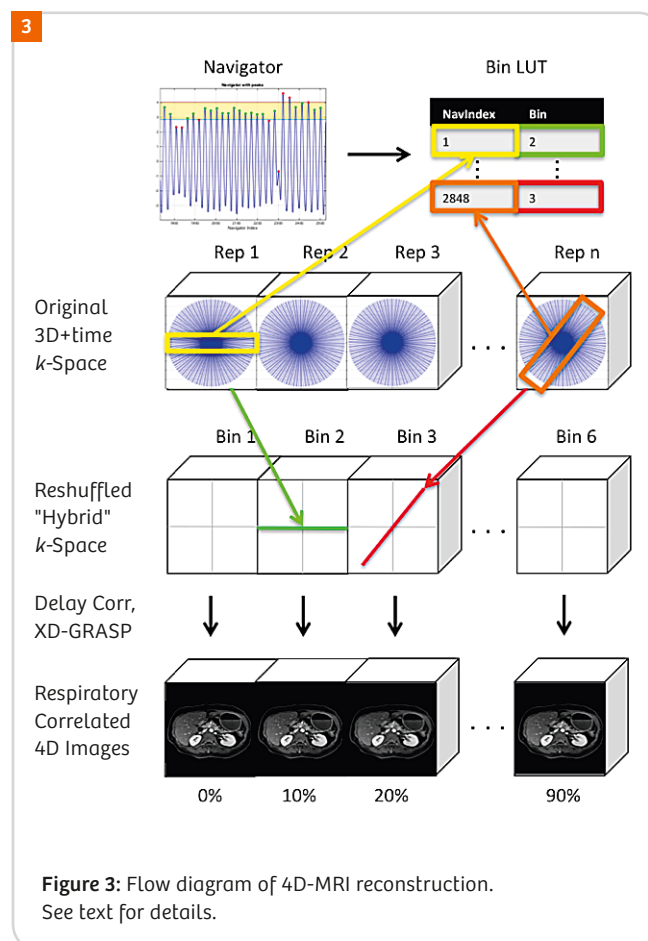
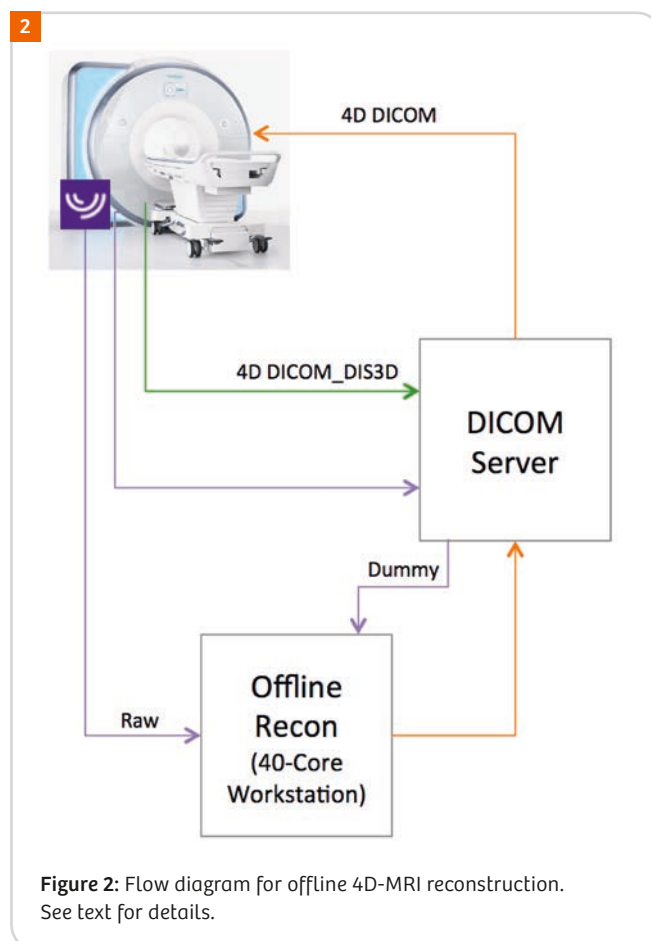
4D-MRI reconstruction pipeline

Figure 2 displays a flow diagram of the 4D-MRI reconstruction pipeline. The raw k -space data were transferred offline

to a 40-core, 2.3 GHz Linux workstation using the Yarra RDS client (<https://yarra.rocks/doc/client/RDS>). In addition, DICOM images from a quick dummy scan, acquired over the same geometrical prescription, were exported to the workstation to facilitate gradient nonlinearity correction. The reconstructed 4D-MR images were converted to DICOM with header information transferred from the dummy scan headers. The 4D-MRI DICOM images were then piped back to the scanner where 3D gradient nonlinearity distortion correction was performed online (orange arrows in Fig. 2). Finally, the distortion corrected 4D-MR images were sent to a clinical delineation software package for use during radiation treatment planning (green arrows in Fig. 2).

4D-MRI reconstruction

4D-MR images were reconstructed in Matlab (The Mathworks, Natick, MA, USA) using the non-uniform fast Fourier transform (NUFFT) toolbox [16]. Projections along the slab-select direction were generated by taking the 1D Fourier transform of the acquired k -space signal passing through the axis of rotation ($k_x = k_y = 0$). One-dimensional motion surrogate signals from all receive coils were generated by plotting the center of mass of each projection, or the cross-correlation coefficient of a given projection against a reference projection as a function of time. These signals were then bandpass filtered between 0.1 and 0.5 Hz



to remove DC offset and high frequency fluctuations (e.g., cardiac motion). Principal component analysis was performed to obtain a single motion surrogate signal using information from all receive coils. This derived navigator signal, analogous to external motion surrogate signals acquired using reflector-camera or respiratory bellows during 4D-CT acquisitions, arises from changes in total signal power during respiration. Constrained amplitude-based sorting was then applied to retrospectively reshuffle each acquired spoke-plane into a hybrid k -space of six-to-eight respiratory phase bins. Correction for gradient and receive chain group delays was performed using an iterative approach [17]. The XD-GRASP algorithm [14, 18], a compressed sensing method exploiting temporal sparsity, was then applied to improve image quality. This process is shown graphically in Figure 3. The Cartesian sampling of the radial stack of stars trajectory was exploited to reduce image reconstruction time by parallelizing over partitions once an initial 1D Fourier transform along the slab-select direction was performed [15].

4D-MRI radiation treatment planning

4D-MR images were loaded into clinical delineation software side-by-side with conventional 4D-CT images sorted based on reflector-camera surrogate. Maximum target motion extents and trajectories were compared between 4D-MRI and 4D-CT. Internal target volumes were constructed on the 4D-CT images and reviewed for agreement on the 4D-MR images.

Results

All patients successfully completed the 2-minute 4D-MRI acquisition. Total reconstruction time was approximately 8 minutes, demonstrating the advantage of the 4D radial

stack-of-stars approach in permitting the reconstruction to be parallelized over partitions. Unlike conventional 4D-CT or other 4D-MRI methods relying on peripheral motion surrogates, no gain resetting or signal saturation was observed in the self-navigated radial stack of stars 4D-MRI motion waveforms used to guide the k -space data reshuffling.

Figure 4 displays one respiratory frame of 4D-CT, and T1-weighted 4D-MR images of a cholangiocarcinoma patient obtained prior to and 20 minutes post-Eovist administration. Consistent with prior studies [14, 15], the XD-GRASP algorithm was effective at reducing undersampling artifacts in the reshuffled pre- and post-contrast 4D-MRI data. The tumor region is more readily discernable on pre and post-Eovist 4D-MR images compared to 4D-CT images. The post-Eovist 4D-MR images also demonstrate a clear demarcation between functioning and dysfunctional hepatocytes.

Figure 5 displays one respiratory frame of 4D-CT and post-Multihance T1-weighted 4D-MR images in a patient with liver metastasis. The liver met is more easily visualized on the 4D-MR images compared to 4D-CT (yellow arrow). In addition, the 4D-MR images do not demonstrate stitching artifacts present on the 4D-CT (evident at the lung-liver interface in the sagittal plane).

Figure 6 displays axial, water-only and fat-only T1-weighted 4D-MR images at inspiratory and expiratory phases for a pancreas cancer patient, obtained using a 4D-MRI Dixon FLASH acquisition. The reconstruction algorithm was effective at separating fat, water, and motion phases.

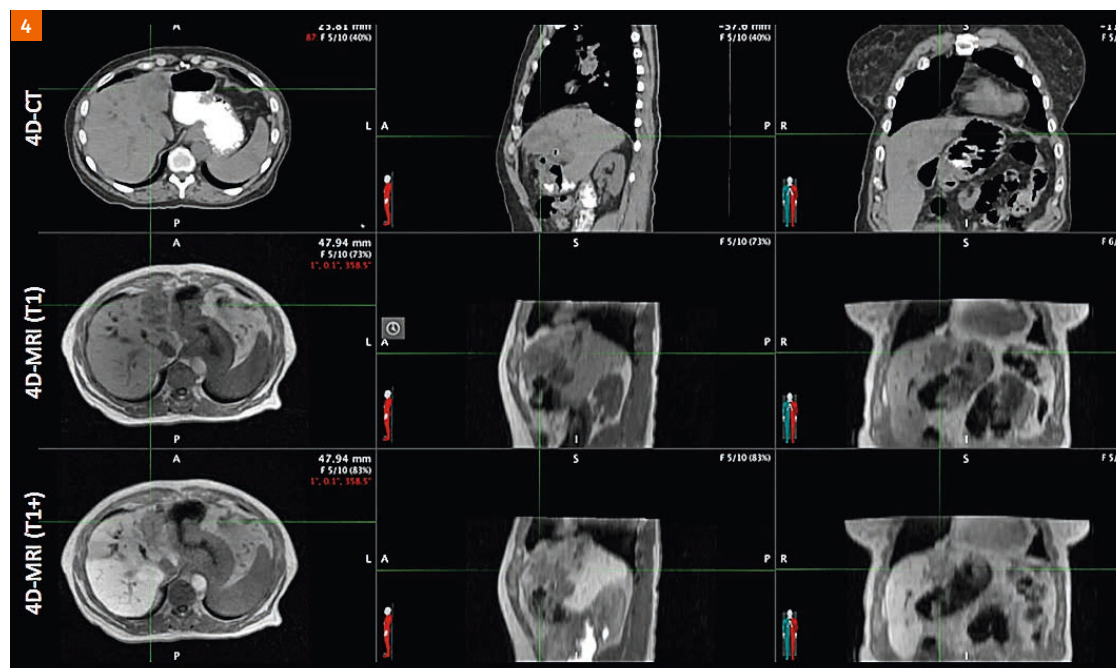


Figure 4: Comparison of 4D-CT (top row) and T1-weighted pre- (middle row) and 20 minute post-Eovist (bottom row) 4D-MR images in a cholangiocarcinoma patient.

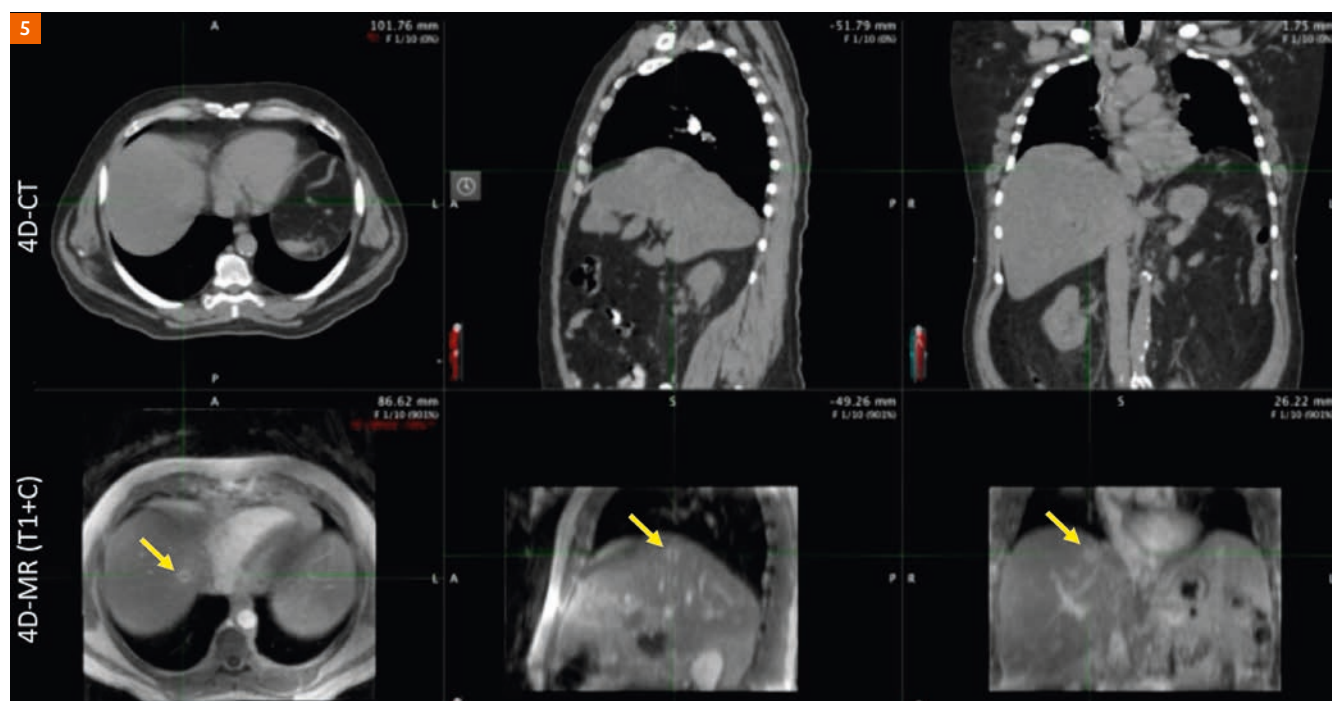


Figure 5: End expiratory 4D-CT (top) and post-Multihance T1-weighted 4D-MR (bottom) images of a liver metastasis patient. The enhancing liver met is more readily visible on the 4D-MR images (yellow arrow).

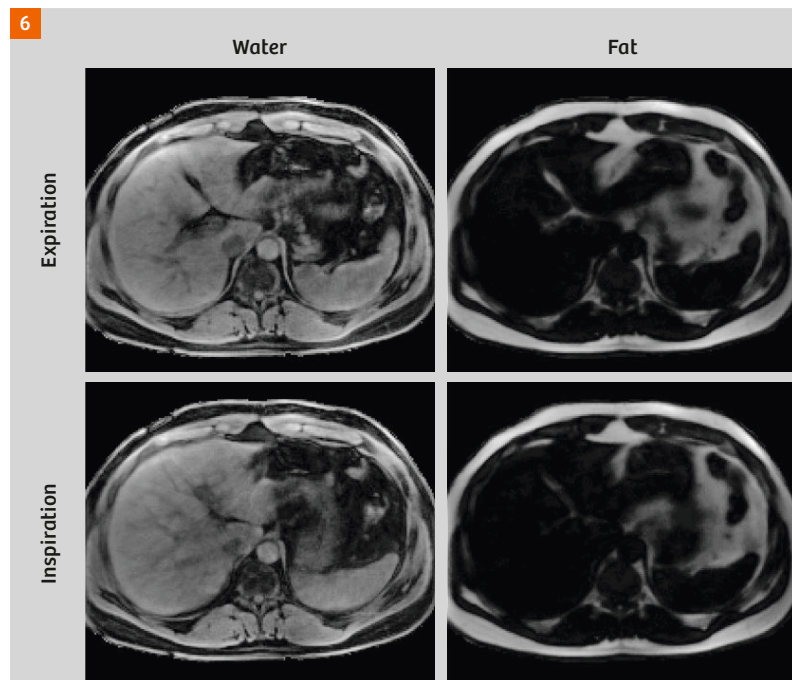


Figure 6: Water-only and fat-only inspiratory and expiratory 4D-MR images of a pancreas cancer patient obtained using a 4D Dixon FLASH acquisition.

Figure 7 displays one respiratory frame of a mixed T2/T1-weighted 4D-MR image obtained in a healthy volunteer using a 4D-MRI PSIF acquisition. Compared to TrueFISP, the PSIF image does not demonstrate banding artifacts but does display increased T2 contrast (evident from the bright cerebrospinal fluid signal).

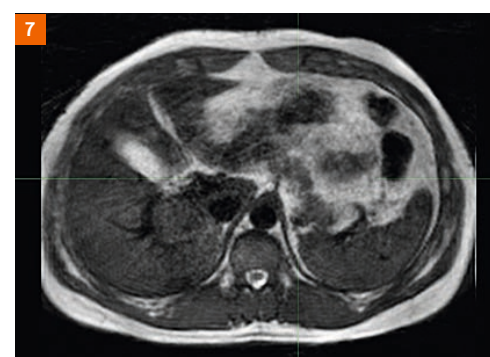


Figure 7: Mixed T2/T1-weighted 4D-MR image of a healthy volunteer acquired using a 4D-MR PSIF acquisition. The increased T2 weighting is evident by the bright CSF signal.

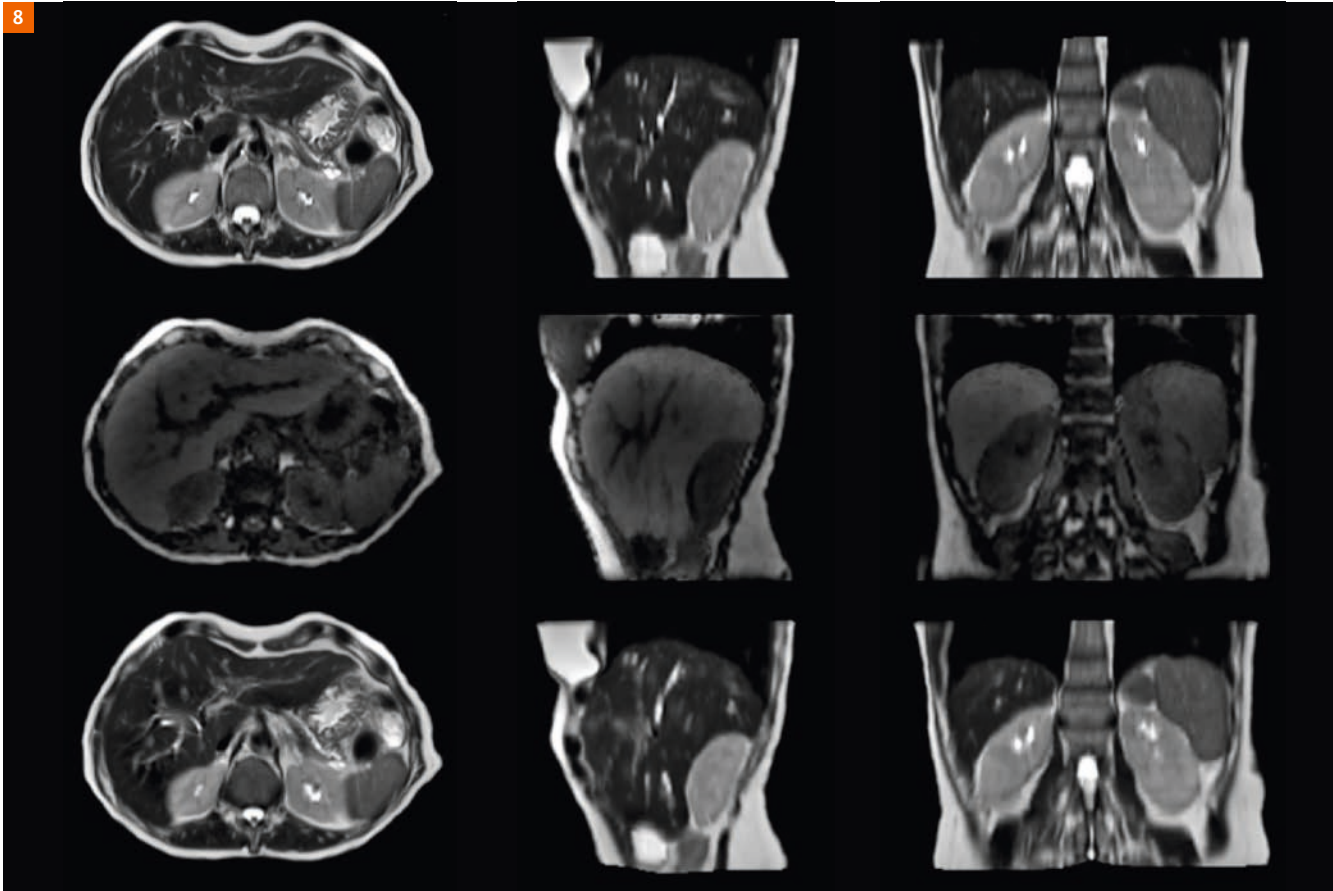


Figure 8: Demonstration of using 4D-MRI as a vehicle. Respiratory-triggered T2 TSE images acquired at end expiration (top row) are transformed to a mid-position anatomical state (middle row) using 4D-MRI and deformable image registration. This process permits image contrasts to be obtained at one respiratory phase more favorable for acquisition, and then transformed to another phase more favorable for treatment delivery (bottom row).

Figure 8 demonstrates the feasibility of using 4D-MRI as a vehicle. In this case, respiratory-triggered T2 images are transformed to a time-averaged, mid-position 4D-MR image [19]. This process permits image contrasts to be acquired at a phase of the respiratory cycle more favorable for acquisition and then be transformed to a potentially different respiratory phase more favorable for treatment delivery.

Discussion

The 4D-MRI method discussed here utilizes the self-navigating properties of radial k -space trajectories to generate respiratory-correlated 4D-MR images. The change in intensity producing the self-navigating signal arises from a change in total signal power in the excited volume during respiration. The method eliminates the need for external respiratory surrogates (bellows, reflector camera, body surface area, etc), and improves image contrast and reduces sorting errors compared to 4D-CT. The spin system steady state is maintained by consecutively exciting the same slab with each shot, and increased efficiency is obtained by

eliminating the need to interlace 1D pencil beam or 2D image navigators. In a prior motion phantom study, the displacement estimates obtained with the 4D-MRI method used here were within 1 mm [15].

We have made several observations during our initial clinical experience of performing and utilizing 4D-MRI for treatment planning:

- 4D-MRI may increase clinical efficiency compared to 4D-CT, depending on the technology available in a particular clinic. The increased efficiencies arise from reduction in setup time for ancillary 4D equipment (respiratory bellows/reflector-camera), (re-)positioning of the equipment, faster acquisition times, and elimination of manual sorting.
- Stitching artifacts that may be present on 4D-CT images are greatly reduced on 4D-MR images. However, in extreme cases of inconsistent breathing patients, respiratory motion inconsistencies can result in a slight blur on 4D-MR images.

- Similar to 4D-CT, the motion waveform derived from the 4D-MR acquisition, and its Fourier transform, can be used to judge whether a given patient may be a candidate for respiratory-gated treatment delivery.
- VIBE interpolation can contribute to blurring along the slab-select direction, which can be reduced by increasing the number of partitions acquired within the slab. Slice partial Fourier can be employed to maintain a high navigator sampling rate in these cases.
- Metal¹ and plastic stents do not appear to significantly obscure 4D-MR image quality.
- Administration of exogenous contrast agents can obscure some structures on non-fat-suppressed T1-weighted 4D-MRI. However, this can be rectified by switching to a 4D-MRI Dixon FLASH acquisition.

The optimal image contrast and timing of the 4D-MRI acquisition within the MR simulation exam may be disease specific. The present 4D-MRI method permits switchable FLASH, FISP, TrueFISP, and PSIF modes, permitting tailoring of 4D image contrast on a tumor-specific basis. Additional studies are planned to determine the optimal 4D-MRI contrast and timing for each cancer site.

References

- 1 Keall PJ, Mageras GS, Balter JM, Emery RS, Forster KM, Jiang SB, Kapatoes JM, Low DA, Murphy MJ, Murray BR, Ramsey CR, Van Herk MB, Vedam SS, Wong JW, Yorke E. The management of respiratory motion in radiation oncology report of AAPM task group 76. *Med Phys* 2006; 33:3874-3900.
- 2 Goldstein SD, Ford EC, Duhon M, McNutt T, Wong J, Herman JM. Use of respiratory-correlated four-dimensional computed tomography to determine acceptable treatment margins for locally advanced pancreatic adenocarcinoma. *Int J Radiat Oncol Biol Phys* 2010; 597-602.
- 3 Njeh CF. Tumor delineation: The weakest link in the search for accuracy in radiotherapy. *J Med Phys* 2008; 33:136-140.
- 4 Blackall JM, Ahmad S, Miquel ME, McClelland JR, Landau DB, Hawkes DJ. MRI-based measurements of respiratory motion variability and assessment of imaging strategies for radiotherapy planning. *Phys Med Biol* 2006; 51:4147-4169.
- 5 Von Siebenthal M, Szekely G, Gamper U, Boesiger P, Lomax A, Cattin Ph. 4D MR imaging of respiratory organ motion and its variability. *Phys Med Biol* 2007; 52:1547-1564.
- 6 Tokuda J, Morikawa S, Haque HA, Tsukamoto T, Matsumiya K, Liao H, Masamune K, Dohi T. Adaptive 4D MR Imaging using Navigator-Based Respiratory Signal for MRI-Guided Therapy. *Mag Reson Med* 2008; 59:1051-1061.
- 7 Cai J, Chang Z, Wang Z, Segars WP, Yin FF. Four-dimensional magnetic resonance imaging (4D-MRI) using image-based respiratory surrogate: A feasibility study. *Med Phys* 2011; 38:6384-6394.
- 8 Hu Y, Caruthers SD, Low DA, Parikh PJ, Mutic S. Respiratory amplitude guided 4-dimensional magnetic resonance imaging. *Int J Radiat Oncol Biol Phys* 2013; 86:198-204.
- 9 Tryggestad E, Flammang A, Han-Oh S, Hales R, Herman J, McNutt T, Roland T, Shea SM, Wong J. Respiration-based sorting of dynamic MRI to derive representative 4D-MRI for radiotherapy planning. *Med Phys* 2013; 40:051909-1 – 051909-12.
- 10 Celicanin Z, Bieri O, Preiswerk F, Cattin P, Scheffler K, Santini F. Simultaneous Acquisition of Image and Navigator Slices using CAIPIRINHA for 4D MRI. *Mag Res Med* 2015; 73:669-676.
- 11 Du D, Caruthers SD, Glide-Hurst C, Low DA, Li HH, Mutic S, and Hu Y. High-Quality T2- Weighted 4-Dimensional Magnetic Resonance Imaging for Radiation Therapy Applications. *Int J Radiat Oncol* 2015; 92:430-437.
- 12 Stemkens B, Tijssen RHN, de Senneville BD, Heerkens HD, van Vulpen M, Lagendijk JJW, and van den Berg CAT. Optimizing 4-dimensional magnetic resonance imaging data sampling for respiratory motion analysis of pancreatic tumors. *Int J Radiat Oncol Biol Phys* 2015; 91:571-8.
- 13 Deng Z, Pang J, Yang W, Yue Y, Sharif B, Tuli R, Li D, Fraass B, and Fan Z. Four- dimensional MRI using three-dimensional radial sampling with respiratory self-gating to characterize temporal phase-resolved respiratory motion in the abdomen. *Magn Reson Med* 2015;
- 14 Feng L, Axel L, Chandarana H, Block KT, Sodickson DK, Otazo R. XD-GRASP: Golden-angle radial MRI with reconstruction of extra motion-state dimensions using compressed sensing. *Magn Reson Med* 2016; 75:775-88.
- 15 Mickevicius NJ, Paulson ES. Investigation of undersampling and reconstruction algorithm dependence on respiratory correlated 4D-MRI for online MR-guided radiation therapy. *Phys Med Biol* 2016; (in press)
- 16 Fessler JA, Sutton BP. Nonuniform fast Fourier transforms using min-max interpolation. *IEEE Trans Sig Proc* 2013; 51:560-574.
- 17 Krämer M, Biermann J, Reichenbach JR. Intrinsic correction of system delays for radial magnetic resonance imaging. *Magn Reson Imag* 2015; 33:491-6
- 18 Benkert T, Feng L, Sodickson DK, Chandarana H, Block KT. Free-breathing volumetric fat/water separation by combining radial sampling, compressed sensing, and parallel imaging. *Magn Reson Med* 2016; (in press)
- 19 Wolthaus JW, Sonke JJ, van Herk M, Belderbos JS, Rossi MM, Lebesque JV, Damen EM. Comparison of different strategies to use four-dimensional computed tomography in treatment planning for lung cancer patients. *Int J Radiat Oncol Biol Phys* 2008; 70:1229-38.

¹ The MRI restrictions (if any) of the metal implant must be considered prior to patient undergoing MRI exam. MR imaging of patients with metallic implants brings specific risks. However, certain implants are approved by the governing regulatory bodies to be MR conditionally safe. For such implants, the previously mentioned warning may not be applicable. Please contact the implant manufacturer for the specific conditional information. The conditions for MR safety are the responsibility of the implant manufacturer, not of Siemens.

Contact



Eric Paulson, Ph.D., DABR
Assistant Professor and Senior
Medical Physicist
Radiation Oncology, Radiology,
and Biophysics

Medical College of Wisconsin
Radiation Oncology
8701 Watertown Plank Road
Milwaukee, WI 53223
USA
epaulson@mcw.edu